An Improved YOLO-SCS Model for AQP4 Antibody Immunofluorescence Image Detection

Xiaoyao Wu [1], Longkuan Shi [1] , Pengju Yin [1, 2] *

[1] School of Mathematics and Physics, Hebei University of Engineering, Handan 056038, China;

[2] Natural Sciences and Science Education, National Institute of Education, Nanyang Technological University, Singapore, 637616, Singapore

* Correspondence: yinpengju@hebeu.edu.cn (P.Y.)

Abstract

Neuromyelitis optica spectrum disorder (NMOSD) diagnosis currently relies on the cell-based assay (CBA) as the gold standard for detecting aquaporin-4 (AQP4) antibodies. However, manual interpretation of AQP4 antibody immunofluorescence images is subjective, time-consuming, and prone to variability. These images often exhibit challenges such as small, densely distributed positive signals, weak fluorescence intensity, and severe background interference from non-specific binding or artifacts.To address these issues, we propose an improved YOLO-based model, termed YOLO-SCS, built upon YOLOv11, for accurate detection of positive signals in AQP4 immunofluorescence images. First, a high-quality dataset of AQP4 immunofluorescence images was constructed with precise annotations. A Gaussian Peak-optimized Channel Adjustment (GPCA) algorithm was designed for preprocessing to enhance weak fluorescence contrast while effectively suppressing background noise. On the YOLOv11 architecture, we incorporated the SPD-Conv module in the downsampling stages to preserve fine-grained spatial features critical for small targets. Additionally, a shape-aware Normalized Wasserstein Distance (NWD) loss function was adopted to improve bounding box regression accuracy for densely overlapping and irregularly shaped positive regions. Experimental evaluations on a clinically representative dataset (positive-to-negative ratio of 1:9) demonstrated superior performance: the proposed YOLO-SCS achieved a positive detection rate of 98.4%, negative specificity of 100%, mAP@0.5 of 0.6971, and mAP@0.5:0.95 of 0.4256. These metrics significantly outperform the baseline YOLOv11 and other state-of-the-art improved models. The model reliably distinguishes specific positive fluorescence signals from background impurities, providing robust automated interpretation support for AQP4 immunofluorescence in NMOSD clinical diagnosis and potentially reducing diagnostic turnaround time and inter-observer variability.

Keywords: AQP4 antibody; immunofluorescence image; target detection; YOLOv11; SPD-Conv; Shape-NWD

Introduction

Neuromyelitis optica spectrum disorder (NMOSD) is a rare but severe autoimmune disorder of the central nervous system, characterized by recurrent attacks of optic neuritis, transverse myelitis, and other debilitating neurological symptoms. Early and accurate diagnosis is critical, as timely initiation of immunosuppressive therapies can prevent irreversible disability and improve long-term outcomes[1-3]. Detection of aquaporin-4 (AQP4) antibodies is a key diagnostic criterion and highly specific biomarker for most NMOSD cases, directly influencing treatment decisions and prognosis. The cell-based assay using indirect immunofluorescence (CBA-IFA) remains the gold standard for AQP4 antibody detection due to its high sensitivity and specificity[1-6]. However, conventional manual interpretation of these immunofluorescence images is labor-intensive, subjective, and prone to inter-observer variability, limiting its scalability in clinical settings and hindering quantitative analysis[7-11].

Despite the rapid progress in deep learning for medical image analysis, automatic interpretation of AQP4 immunofluorescence images remains underdeveloped[12, 13]. Existing object detection models often struggle with the domain-specific challenges of these images: positive signals manifest as small, densely overlapping membrane patterns on astrocytes; fluorescence intensity is frequently weak; and non-specific background

fluorescence, impurities, and artifacts introduce severe interference. These factors lead to frequent missed detections, false positives, and poor localization accuracy in standard models, including recent YOLO variants[14, 15]. Previous applications of deep learning to immunofluorescence or cell detection have primarily focused on brighter, larger, or less noisy targets (e.g., blood cells or general microscopy), leaving a clear gap in handling the subtle, dense, and noisy characteristics unique to AQP4 antibody patterns[16, 17]. To bridge this gap, the present study targets the automated and reliable detection of positive AQP4 signals in real-world clinical immunofluorescence images[18-27]. The core objective is to develop a robust object detection model capable of accurately identifying weak, small, and densely distributed positive regions while effectively suppressing background noise and artifacts, thereby supporting faster, more consistent, and quantitative AQP4 antibody interpretation for NMOSD diagnosis[28-30].

We first collaborated with clinical experts to acquire thousands of authentic patient immunofluorescence images via automated imaging systems and carefully annotated approximately 1,000 representative images, precisely delineating positive signals, background signals, ambiguous areas, and impurities to create a high-quality, clinically representative dataset[31, 32]. For preprocessing, we designed a Gaussian Peak-optimized Channel Adjustment (GPCA) algorithm that combines Gaussian filtering and adaptive thresholding to enhance weak fluorescence contrast and suppress noise. Building on YOLOv11, which is the latest version offering optimized feature extraction and fusion. we propose YOLO-SCS, an enhanced model incorporating two key innovations: (1) integration of the SPD-Conv module in downsampling layers to preserve fine-grained spatial details essential for small targets, and (2) adoption of a shape-aware Normalized Wasserstein Distance (NWD) loss function to improve bounding box regression precision for densely overlapping and irregularly shaped positive regions. The paper is organized as follows: Section 1 introduces the dataset construction, design, and preprocessing algorithm. Section 2 details the YOLO-SCS architecture. Section 3 presents the analysis of the results. Section 4 summarizes the content of this paper.

1. Literature Review

1.1 Data Acquisition

The experimental data are derived from real clinical detection samples provided by Shaanxi Maiyuan Biotechnology Co., Ltd., and all images are collected by the self-developed fully automatic immunofluorescence slide scanning equipment of the company. The sample types include serum and cerebrospinal fluid of clinically diagnosed or suspected NMOSD patients, covering different antibody titer levels and various typical fluorescent forms. The resolution of all original images is 2592×1944 pixels, and the format is lossless TIFF or high-fidelity JPG to retain the microscopic detail information to the maximum extent. The dataset includes a total of 7164 images, among which 1478 are typical positive images, 5517 are typical negative images and 169 are weak positive images.

1.2 Data Annotation

To ensure high-quality ground truth for training and evaluation, experienced clinical laboratory experts were invited to guide the annotation process. A fine-grained multi-class labeling strategy was adopted to mitigate model misjudgments caused by complex background interference, non-specific fluorescence, and artifacts commonly encountered in real-world AQP4 immunofluorescence images[33, 34]. The open-source annotation tool LabelImg was employed for manual bounding-box labeling, enabling pixel-level precise rectangular annotations of various image elements. As illustrated in **Figure 1**, four distinct categories were defined to comprehensively capture the image content: Category 0 for background fluorescence (non-specific or weak diffuse signals), Category 1 for positive cells (specific membrane-pattern fluorescence indicating AQP4 antibody binding), Category 2 for impurities and stains (artifacts, debris, or contamination), and Category 3 for ambiguous/low-quality regions (blurry, overexposed, or uncertain areas). A total of approximately 1,000 high-resolution, high-cell-density immunofluorescence images were meticulously annotated. These images were selected from

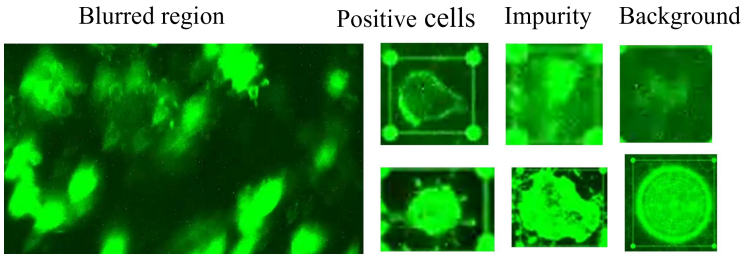

Figure 1. Classification and Examples of Marked Signals

thousands of real patient samples collected using automated imaging equipment, ensuring clinical representativeness and diversity in positive-to-negative ratios, fluorescence intensity variations, and interference levels. To maintain balanced class distributions and guarantee objective model evaluation, the annotated dataset was divided into training, validation, and test sets using a stratified sampling approach with a ratio of 7:2:1. Stratification was performed based on the proportion of each annotation category and overall positivity status, preventing distribution bias across subsets and enhancing the reliability of performance metrics. This carefully constructed dataset, with expert-supervised multi-class annotations, provides a robust

foundation for addressing the challenges of small, dense, weak, and noisy positive signals in AQP4 immunofluorescence detection.

1.3 Image Preprocessing: Gaussian Peak-optimized Channel Adjustment

AQP4 immunofluorescence images frequently exhibit low contrast, non-uniform illumination, and severe background noise interference due to inherently weak fluorescence signals, non-specific binding, and various imaging artifacts[35-40]. Conventional contrast enhancement methods, such as histogram equalization, tend to over-amplify background noise or fail to selectively preserve the subtle membrane patterns characteristic of positive cells, often resulting in reduced signal-to-noise ratio or loss of diagnostically relevant structural details.

To address these challenges more effectively, we propose the Gaussian Peak-optimized Channel Adjustment (GPCA) algorithm, a specialized preprocessing technique developed specifically for AQP4 immunofluorescence images. Statistical examination of brightness histograms from a large collection of such images consistently reveals a bimodal or multimodal distribution: a prominent low-brightness peak corresponds to the extensive dark background, while one or more higher-brightness peaks represent the foreground fluorescence signals, primarily associated with membrane-bound positive patterns.

The GPCA algorithm operates through three integrated steps (**Figure 2**). First, Gaussian smoothing and histogram continuization are applied by convolving the one-dimensional brightness histogram of the input image with a Gaussian kernel. This process suppresses minor fluctuations induced by discrete noise and quantization artifacts, converting the jagged discrete histogram into a smooth, continuous density function that facilitates precise localization of peak centers[41-43]. Second, peak detection and interval partitioning are performed using an automated peak-finding algorithm on the smoothed histogram. The initial major peak is designated as the background mode (reflecting average noise intensity), while subsequent prominent peaks indicate the effective fluorescence signal modes, thereby establishing critical intensity thresholds to separate background, transitional, and signal-dominant regions. Third, an adaptive piecewise linear gray-level mapping function is constructed from these peak positions. Pixels below the background peak threshold are strongly suppressed (mapped close to zero) to eliminate diffuse autofluorescence and non-specific noise; intensities in the vicinity of the signal peak undergo non-linear stretching with a steeper mapping slope to selectively enhance the contrast and edge sharpness of weak positive membrane signals; and high-intensity outliers, such as saturated noise or bright artifacts, are clipped to maintain dynamic range balance and prevent over-enhancement.

By leveraging the characteristic histogram peaks in an adaptive, data-driven manner, GPCA effectively suppresses background autofluorescence, substantially improves the clarity and sharpness of positive cell membrane edges, and concurrently optimizes color balance and signal-to-noise ratio across channels. This results in cleaner, higher-contrast input images that retain critical structural details, thereby providing significantly enhanced input quality for subsequent deep learning-based object detection models, especially in scenarios involving small, densely distributed, low-intensity targets amid complex clinical interference.

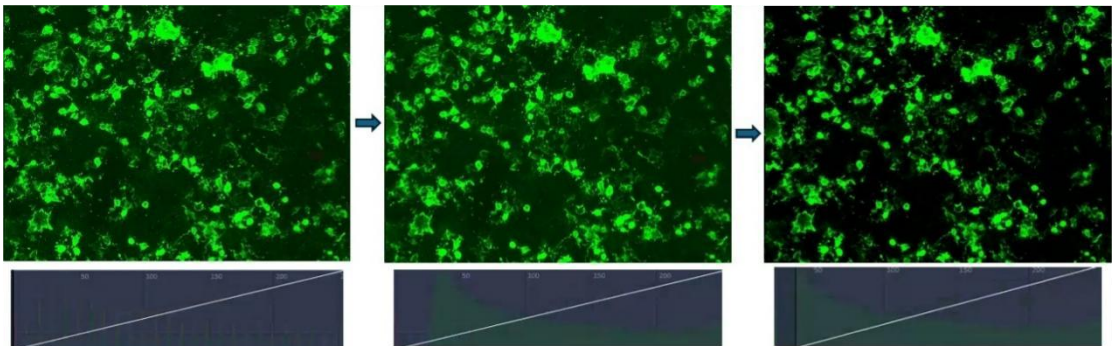

Original image | After Gaussian filtering | After processing with the adaptive threshold method for peak-seeking

Figure 2. Step-by-step effect display of GPCA processing of fluorescence images

2. YOLO-SCS Model Design

The proposed YOLO-SCS model takes YOLOv11 as its foundational architecture, chosen for its excellent trade-off between real-time inference speed and high detection accuracy in challenging visual scenarios[44-48]. Building on previous versions, YOLOv11 introduces several important refinements, including the more efficient C3k2 block in the backbone to improve feature representation while reducing computational cost, an optimized Path Aggregation Network in the neck for better multi-scale feature integration, and enhanced attention mechanisms that strengthen global context perception without sacrificing millisecond-level processing speed[18-23]. These advancements render YOLOv11 highly suitable for high-throughput clinical tasks such as the automated interpretation of AQP4 immunofluorescence images. Nevertheless, when applied directly to this specific domain, the original YOLOv11 encounters notable shortcomings. The tiny membrane-pattern fluorescence signals of positive cells, often only a few pixels in width, suffer substantial feature loss during

conventional downsampling operations, frequently resulting in missed detections of weak positive signals. Additionally, the dense overlapping arrangement of HEK-293 cells in these images leads to poor bounding box regression accuracy, manifesting as boundary drift, duplicate predictions, or incomplete localization of targets.

To overcome these domain-specific difficulties, the YOLO-SCS model incorporates two principal modifications. The first is the integration of the Space-to-Depth Convolution module, known as SPD-Conv, which is strategically embedded into selected downsampling layers of the backbone network to achieve lossless resolution reduction. In SPD-Conv, an input feature map X with dimensions S × S × C_1 undergoes a Space-to-Depth rearrangement with scale factor s (commonly s=2), which partitions the spatial dimensions into s^2 sub-maps and concatenates them along the channel axis, producing an intermediate feature map of size S/s × S/s × s^2C_1. This operation downsamples spatially while preserving every original pixel value, circumventing the irreversible information discard typical of strided convolution or pooling (**Figure 3**). A subsequent non-strided convolution layer then adjusts the channel dimension to C_2 and performs feature refinement, yielding the output Y with dimensions S/s × S/s × C_2. By placing SPD-Conv modules at critical downsampling positions, the model retains richer low-level texture and edge information vital for detecting small and weakly fluorescent positive signals, thereby markedly improving recall performance in low-contrast and small-target conditions.

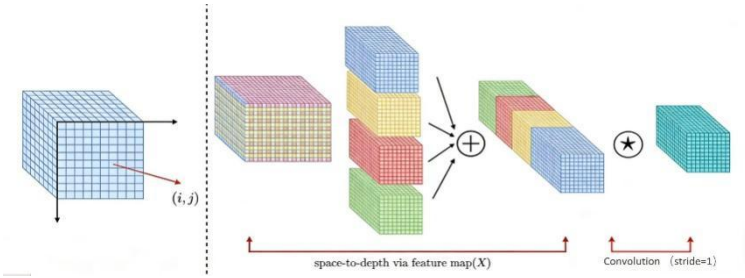

Figure 3. SPD-Conv Module.

The second key improvement addresses the regression challenges in densely packed cell regions by replacing the conventional IoU-based regression loss with the Shape-aware Normalized Wasserstein Distance loss, referred to as Shape-NWD. This loss treats each bounding box as a two-dimensional Gaussian distribution N(μ, Σ), where μ represents the center coordinates and Σ is the covariance matrix derived from the box width and height. The squared Wasserstein distance between two such modeled boxes A and B is calculated as :

$$W_2^2(A,B)=\|\mu_A-\mu_B\|_2^2+\|\Sigma_A^{\frac{1}{2}}-\Sigma_B^{\frac{1}{2}}\|_F^2 \quad (1)$$

which simultaneously quantifies positional deviation and shape dissimilarity in a geometrically interpretable manner. The Normalized Wasserstein Distance is then obtained through an exponential mapping:

$$\mathrm{NWD}(A,B)=exp\left(0-\frac{W_2^2(A,B)}{C}\right) \quad (2)$$

where C is a tunable constant that controls the sensitivity scale. The Shape-NWD loss, typically formulated as 1 − NWD(A, B), delivers smooth and continuous gradients even when boxes exhibit minimal or no overlap, enabling more precise adjustments to both position and shape during training. This probabilistic modeling approach significantly alleviates issues such as detection drift, duplication, and missed targets in dense cell clusters.

The overall structure of YOLO-SCS follows the classic YOLO pipeline while seamlessly incorporating these enhancements (**Figure 4**). Preprocessed AQP4 images, enhanced by the GPCA algorithm, are first resized to a uniform 640×640 resolution, normalized, and subjected to Mosaic data augmentation during training to boost robustness against variations in scale, illumination, and background interference. The feature extraction backbone, built on the refined YOLOv11 design with C3k2 blocks, extracts multi-scale features, with SPD-Conv modules inserted at key downsampling stages to safeguard small-target details and multi-scale pooling combined with separable convolutions to suppress background impurities. In the neck, the optimized PANet conducts bidirectional fusion: top-down pathways propagate high-level semantic information to lower-resolution maps, while bottom-up pathways aggregate precise positional and shape cues from shallow layers, thereby strengthening the representation of both small and densely clustered targets. Finally, the prediction head processes the fused multi-scale features to output bounding box coordinates, objectness confidence scores, and class probabilities. During training, the Shape-NWD loss guides regression optimization in conjunction with standard classification and objectness losses, and at inference, non-maximum suppression is applied to produce accurate final detections of positive fluorescence signals.

Through the synergistic combination of lossless downsampling via SPD-Conv and robust dense-target regression via Shape-NWD, YOLO-SCS achieves substantially improved performance in identifying weak, small, and densely distributed positive signals within the complex environment of AQP4 immunofluorescence images, establishing a solid technical foundation for automated support in NMOSD clinical diagnosis.

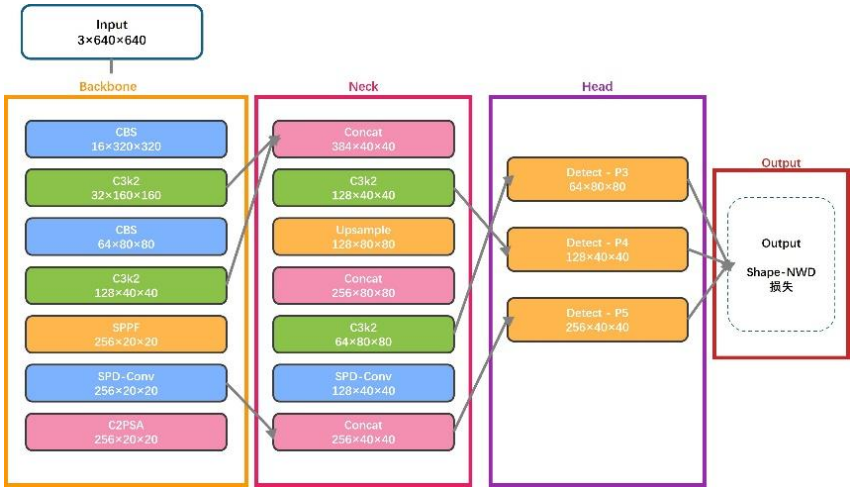

Figure 4. Framework of the YOLO-SCS model

3 Experimental Design and Result Analysis

3.1 Experimental Setup

All experiments were performed in a unified hardware and software environment to ensure reproducibility and comparability of results. The computational platform was equipped with an NVIDIA RTX 4000 GPU featuring 24 GB of video memory. The software environment utilized Python 3.8 and the PyTorch deep learning framework. Model training adopted the following key hyperparameters: a batch size of 16, an initial learning rate of 0.01, a final learning rate of 0.001 under a one-cycle scheduling policy, the SGD optimizer with standard momentum and weight decay, and a total of 200 epochs (**Figure 5a-c**). Hyperparameter optimization, including the kernel size of the SPD-Conv module, was conducted through systematic grid search and ablation experiments. The optimal convolution kernel size was determined to be 3×3, which effectively captures fine details of small fluorescent membrane patterns while preventing unnecessary increases in computational complexity from larger kernels.

3.2 Training Convergence and Validation Performance

The training process was tracked using validation set metrics, which showed rapid initial gains in performance followed by gradual stabilization. The mAP@0.5 curve rose sharply in the early epochs and exhibited progressively smaller fluctuations as training continued. Peak performance was reached around epoch 190, with mAP@0.5 attaining 0.68 and mAP@0.5:0.95 reaching 0.40 on the validation set. Given the inherent challenges of AQP4 immunofluorescence detection—including very small, densely clustered targets, weak fluorescence signals, and substantial background interference—these values are considered strong and align with or surpass the accuracy thresholds typically accepted by clinical experts for auxiliary diagnostic purposes. The confusion matrix on the validation set further demonstrated reliable classification of the primary target class (AQP4-positive cells) with accuracy consistently above 92%. For secondary classes encompassing background fluorescence, impurities, stains, and ambiguous regions, precision hovered around or above 90%, confirming the model's capability to effectively differentiate true positive signals from non-specific noise and artifacts. This robust positive cell identification accuracy provides a dependable quantitative foundation for downstream sample-level interpretation.

3.3 Sample-Level Positive/Negative

Interpretation Rule In standard clinical AQP4 immunofluorescence assays, samples undergo serial dilution to ensure the fluorescent signal falls within the microscope's optimal dynamic range. Consequently, the count and density of positive cells at a fixed dilution serve as the principal quantitative criteria for sample classification. Combining the model's detection outputs with insights from experienced clinical readers, a practical two-stage interpretation rule was established. Initially, all predicted bounding boxes are filtered by confidence score, retaining only those with confidence ≥ 0.5 as valid positive signals to suppress low-confidence background interference. The number of retained positive cells (N_pos) per image is then used for final judgment: samples with N_pos ≥ 10 are classified as typical positive, characterized by abundant and distinctly membrane-patterned fluorescence with high diagnostic specificity; samples with N_pos < 3 are classified as typical negative, consistent with minimal or absent specific fluorescence; and samples with $3 \leq$ N_pos < 10 are designated as suspicious, indicating potential borderline weak positivity or prominent non-specific interference, and are automatically flagged for manual expert review to reduce the risk of diagnostic error.

3.4 Performance on Independent

Test Sets To evaluate generalization and clinical relevance, two distinct test sets were constructed. The first, a balanced set with equal proportions of positive and negative samples, was designed to assess the model's peak discriminative ability without class imbalance effects. On this set, YOLO-SCS

achieved 99.1% accuracy for positive samples and 100% accuracy for negative samples, reflecting near-perfect detection of specific fluorescent patterns and negligible false positives in non-fluorescent regions. The second test set mirrored real-world NMOSD screening conditions, with a positive-to-negative ratio of approximately 1:9. Despite the extreme rarity of positive cases, the model sustained high performance, attaining a positive detection rate (sensitivity) of 98.4%—with only rare misses on extremely weak signals and maintaining 100% negative specificity (**Table 1**). These results underscore the model's resilience to severe class imbalance and complex background clutter, positioning it as a reliable tool for large-scale clinical screening where overlooking rare positives must be strictly minimized.

Table 1. Classification results

Origin\Predicted	positive	doubt	negative	total	Accuracy (%)
positive	240	6	4	250	98.4
negative	0	90	2160	2250	100

3.5 Comparison with State-of-the-Art Models

To validate the superiority of YOLO-SCS, it was benchmarked against several leading object detection models under identical experimental conditions. The compared methods included the baseline YOLOv11, the more recent YOLOv12, as well as task-oriented variants such as FEM-YOLO (feature enhancement module), MSCAA-YOLO (multi-scale context aggregation attention), and AKConv-YOLO (adaptive kernel convolution) (**Figure 5d**). Evaluation encompassed both detection-level metrics (mAP@0.5 and mAP@0.5:0.95) and sample-level positive/negative classification accuracy. YOLO-SCS outperformed all baselines, achieving mAP@0.5 of 0.6971 and mAP@0.5:0.95 of 0.4256—approximately 10% higher than vanilla YOLOv11 (**Table 2**).

These gains are largely attributed to the SPD-Conv module's preservation of tiny fluorescent features during downsampling and the Shape-NWD loss's improved regression precision in dense cell areas. At the sample classification level, YOLO-SCS recorded 98.9% positive accuracy and 100% negative accuracy. In comparison, FEM-YOLO and MSCAA-YOLO provide general feature and context improvements but still show higher miss rates on very weak signals. YOLOv12, while featuring advanced attention mechanisms, lacks domain-specific adaptations for AQP4 image characteristics and underperforms accordingly. AKConv-YOLO offers kernel adaptability but falls short in addressing small-target feature retention and dense-overlap regression. Overall, YOLO-SCS achieves a notable advancement in both precise localization and reliable clinical decision-making while preserving efficient inference, making it a promising core component for automated AQP4 immunofluorescence interpretation in NMOSD diagnostics.

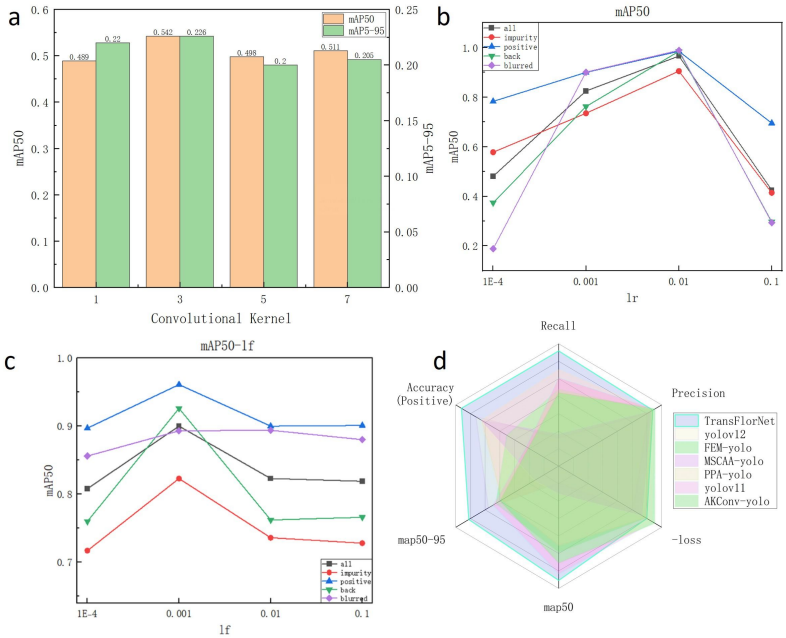

Fig 5. Analysis of Recognition Results. (a). Adjustment of convolution kernel function. (b-c) Adjustment of parameters for lr and lf. (d) Comparison of Model Performances.

Table 2. Comparative test

Model	Recall	Precision	loss	map50	map50-95	Accuracy(P)	Accuracy(N)
YOLO-SCS	0.63589	0.69129	0.31871	0.69714	0.42562	98.9%	100%
yolov12	0.58610	0.49393	0.50607	0.52761	0.25104	96.1%	99.2%
FEM-yolo	0.61398	0.50998	0.49002	0.55876	0.24659	90.1%	98.5%
MSCAA-yolo	0.58845	0.50564	0.49436	0.53242	0.22406	95.2%	95.7%
PPA-yolo	0.62521	0.51010	0.48990	0.55582	0.24321	95.0%	98.9%
yolov11	0.62057	0.51939	0.48061	0.56851	0.24830	86.3%	99.6%
AKConv-yolo	0.61201	0.52168	0.47832	0.56358	0.24416	85.9%	99.2%

4 Conclusion

This study focuses on the technical challenges of AQP4 antibody immunofluorescence image detection for NMOSD diagnosis, such as dense small targets, weak fluorescence signals and severe background interference, as well as the subjectivity and inefficiency of manual interpretation. An improved YOLO-SCS model based on YOLOv11 is proposed, and a targeted technical scheme covering dataset building, image preprocessing and model optimization is constructed to realize automated and accurate detection of positive signals in such images.

A clinically representative AQP4 immunofluorescence image dataset including positive, negative and weak positive samples was constructed, and fine-grained multi-class annotation was completed under the guidance of clinical experts. Aiming at the low contrast and high noise of original images, the GPCA preprocessing algorithm was designed. This algorithm mines the histogram distribution characteristics of images to effectively enhance the contrast of weak fluorescence signals and suppress background noise, laying a solid data foundation for subsequent model training.

On the basis of YOLOv11, the YOLO-SCS model has two key improvements. The SPD-Conv module is embedded in the downsampling layer to achieve lossless resolution reduction and preserve the fine spatial features of small targets, which solves the problem of feature loss in traditional downsampling. The traditional IoU loss is replaced with the Shape-NWD loss function, which models bounding boxes as two-dimensional Gaussian distributions to optimize the regression accuracy of densely overlapping and irregular targets, thus reducing detection drift and missed detection.

Experimental results on the test set with a clinically realistic positive-to-negative ratio of 1:9 show that the YOLO-SCS model achieves a 98.4% positive detection rate and 100% negative specificity, with mAP@0.5 and mAP@0.5:0.95 reaching 0.6971 and 0.4256 respectively. The model significantly outperforms the baseline YOLOv11 and other state-of-the-art improved models, and can accurately distinguish positive fluorescence signals from background impurities and non-specific interference, showing high clinical reliability. The YOLO-SCS model provides an effective technical solution for the automated interpretation of AQP4 immunofluorescence images, which is of great clinical value for the early and accurate diagnosis of NMOSD and is expected to reduce diagnostic turnaround time and inter-observer variability. Future research will focus on multi-modal data fusion by combining clinical text and medical imaging data to improve the model's diagnostic accuracy and generalization ability. Meanwhile, model lightweight transformation will be carried out to realize deployment on portable detection equipment and further expand its clinical application scenarios.

Declaration of competing interest

The authors declare that they have no known competing financial interests or personal relationships that could have appeared to influence the work reported in this paper.

REFERENCES

1. ABDULRAHMAN Z, HENDRIKS N, KRUSE A J, et al. Immune-based biomarker accurately predicts response to imiquimod immunotherapy in cervical high-grade squamous intraepithelial lesions [J]. JOURNAL FOR IMMUNOTHERAPY OF CANCER, 2022, 10(11).
2. ALESSI J V, LINDSAY J R, GIOBBIE-HURDER A, et al. Immunoprofiling at an Institutional Scale Reveals That High Numbers of Intratumoral CD8+ and PD-1+ Cells Predict Superior Patient Survival Across Major Cancer Types Independent of Major Risk Factors [J]. JCO PRECISION ONCOLOGY, 2025, 9.
3. ANDRIC F, AL-FAIROUZI A, WETTERGREN Y, et al. Immune Microenvironment in Sporadic Early-Onset versus Average-Onset Colorectal Cancer [J]. CANCERS, 2023, 15(5).

4. AUNG T N, SHA S B, WILMOTT J S, et al. Objective assessment of tumor infiltrating lymphocytes as a prognostic marker in melanoma using machine learning algorithms [J]. EBIOMEDICINE, 2022, 82.
5. AZIMI M. From Spatial Patterns to Prognosis: Decoding Single-Cell Architecture in Cancer with Hyperplex Immunofluorescence Imaging [J]. JOURNAL OF CANCER, 2025, 16(12): 3654-3663.
6. BAI R L, JIA Y H, WANG B, et al. In vivo spatiotemporal mapping of proliferation activity in gliomas via water-exchange dynamic contrast-enhanced MRI [J]. THERANOSTICS, 2025, 15(10): 4693-707.
7. WANG Q, HUANG Y X, ZHANG Y, et al. Digital pathology-based prognostic model for hepatocellular carcinoma: Integrating pathomics signatures with clinical parameters for recurrence prediction and biological interpretation [J]. COMPUTER METHODS AND PROGRAMS IN BIOMEDICINE, 2026, 275.
8. WATSON S S, DUC B, KANG Z Q, et al. Microenvironmental reorganization in brain tumors following radiotherapy and recurrence revealed by hyperplexed immunofluorescence imaging [J]. NATURE COMMUNICATIONS, 2024, 15(1).
9. WESSELINK E, THOMAS C E, TAKASHIMA Y, et al. Associations between Calcium Intake and T-cell Infiltration in Colorectal Tumors [J]. CANCER PREVENTION RESEARCH, 2025, 18(9): 561-571.
10. XIE T, XUE H C, HUANG A L, et al. Integrating multi-omics data with artificial intelligence to decipher the role of tumor-infiltrating lymphocytes in tumor immunotherapy [J]. PATHOLOGY RESEARCH AND PRACTICE, 2025, 271.
11. YANG C K, LEE C Y, WANG H S, et al. Glomerular disease classification and lesion identification by machine learning [J]. BIOMEDICAL JOURNAL, 2022, 45(4): 675-685.
12. BAUCKNEHT M, MARINI C, COSSU V, et al. Gene's expression underpinning the divergent predictive value of [18F]F-fluorodeoxyglucose and prostate-specific membrane antigen positron emission tomography in primary prostate cancer: a bioinformatic and experimental study [J]. JOURNAL OF TRANSLATIONAL MEDICINE, 2023, 21(1).
13. BERTIN D, BONGRAND P, BARDIN N. Comparison of the Capacity of Several Machine Learning Tools to Assist Immunofluorescence-Based Detection of Anti-Neutrophil Cytoplasmic Antibodies [J]. INTERNATIONAL JOURNAL OF MOLECULAR SCIENCES, 2024, 25(6).
14. BOROWSKY J, HARUKI K, LAU M C, et al. Association of Fusobacterium nucleatum with Specific T-cell Subsets in the Colorectal Carcinoma Microenvironment [J]. CLINICAL CANCER RESEARCH, 2021, 27(10): 2816-2826.
15. CAI S Y, HU T, VENKATESAN M, et al. Multiplexed protein profiling reveals spatial subcellular signaling networks [J]. ISCIENCE, 2022, 25(9).
16. CHEN Y, CHEN Y Y, FU S S, et al. VGG16-based intelligent image analysis in the pathological diagnosis of IgA nephropathy [J]. JOURNAL OF RADIATION RESEARCH AND APPLIED SCIENCES, 2023, 16(3).
17. COSSELLU D, VIVADO E, BATTI L, et al. Volumetric atlas of the rat inner ear from microCT and iDISCO plus cleared temporal bones [J]. PEERJ, 2025, 13.
18. MENCATTINI A, TOCCI T, NUCCETELLI M, et al. Automatic classification of HEp-2 specimens by explainable deep learning and Jensen-Shannon reliability index [J]. ARTIFICIAL INTELLIGENCE IN MEDICINE, 2025, 160.
19. MUNTINGA C L P, VAN STEENWIJK P J D, KOOREMAN L F S, et al. Pre-existing infiltration with T cells and CD14+myeloid cells is associated with treatment response to imiquimod in primary and recurrent vulvar high-grade squamous intraepithelial lesions [J]. JOURNAL FOR IMMUNOTHERAPY OF CANCER, 2025, 13(10).
20. NESBIT M, MAMO J C, MAJIMBI M, et al. Automated Quantitative Analysis of ex vivo Blood-Brain Barrier Permeability Using Intellesis Machine-Learning [J]. FRONTIERS IN NEUROSCIENCE, 2021, 15.
21. QIN Y, HUTTLIN E L, WINSNES C F, et al. A multi-scale map of cell structure fusing protein images and interactions [J]. NATURE, 2021, 600(7889): 536-541.
22. RODRIGUEZ S G D, HERRERA P H, FLORES C A, et al. A Machine Learning Workflow of Multiplexed Immunofluorescence Images to Interrogate Activator and Tolerogenic Profiles of Conventional Type 1 Dendritic Cells Infiltrating Melanomas of Disease-Free and

Metastatic Patients [J]. JOURNAL OF ONCOLOGY, 2022, 2.

23. ROJAS F, HERNANDEZ S, LAZCANO R, et al. Multiplex Immunofluorescence and the Digital Image Analysis Workflow for Evaluation of the Tumor Immune Environment in Translational Research [J]. FRONTIERS IN ONCOLOGY, 2022, 12.
24. SCHWARZE S, SCHAADT N S, SOBOTTA V M G, et al. Task design for crowdsourced glioma cell annotation in microscopy images [J]. SCIENTIFIC REPORTS, 2024, 14(1).
25. SHISHIDO S N, COURCOUBETIS G, KUHN P, et al. Automated Single-Cell Analysis in the Liquid Biopsy of Breast Cancer [J]. CANCERS, 2025, 17(17).
26. SUN A X, HAYAT H, LIU S H, et al. 3D in vivo Magnetic Particle Imaging of Human Stem Cell-Derived Islet Organoid Transplantation Using a Machine Learning Algorithm [J]. FRONTIERS IN CELL AND DEVELOPMENTAL BIOLOGY, 2021, 9.
27. TUOMISTO A, SIRNIö P, ELOMAA H, et al. Integrating Tumor Intraepithelial CD8+and Stromal FOXP3+T-Cell Densities as an Enhanced Immune Prognostic Index in Colorectal Cancer [J]. LABORATORY INVESTIGATION, 2025, 105(11).
28. GAVRIEL C G, DIMITRIOU N, BRIEU N, et al. Assessment of Immunological Features in Muscle-Invasive Bladder Cancer Prognosis Using Ensemble Learning [J]. CANCERS, 2021, 13(7).
29. GORMAN C, PUNZO D, OCTAVIANO I, et al. Interoperable slide microscopy viewer and annotation tool for imaging data science and computational pathology [J]. NATURE COMMUNICATIONS, 2023, 14(1).
30. HIRWAY S U, HASSAN N T, SOFRONIOU M, et al. Immunofluorescence Image Feature Analysis and Phenotype Scoring Pipeline for Distinguishing Epithelial-Mesenchymal Transition [J]. MICROSCOPY AND MICROANALYSIS, 2021, 27(4): 849-859.
31. JI X N, LI Q Y, LIU Z P, et al. Identification of Active Components for Sports Supplements: Machine Learning-Driven Classification and Cell-Based Validation [J]. ACS OMEGA, 2024, 9(10): 11347-11355.
32. JIA Y, YUAN L, WEN W J, et al. Circulating proteins and metabolites panel for noninvasive preoperative diagnosis of epithelial ovarian cancer [J]. BMC MEDICINE, 2025, 23(1).
33. JIN Y Y, BRENNECKE J, SODMANN A, et al. Antibody selection and automated quantification of TRPV1 immunofluorescence on human skin [J]. SCIENTIFIC REPORTS, 2024, 14(1).
34. KATARAS T J, JANG T J, KOURY J, et al. ACCT is a fast and accessible automatic cell counting tool using machine learning for 2D image segmentation [J]. SCIENTIFIC REPORTS, 2023, 13(1).
35. KEIKHOSRAVI A, ALMANSOUR F, BOHRER C H, et al. High-throughput image processing software for the study of nuclear architecture and gene expression [J]. SCIENTIFIC REPORTS, 2024, 14(1).
36. JIMéNEZ-SáNCHEZ D, ARIZ M, DE ANDREA C E, et al. Synplex: In Silico Modeling of the Tumor Microenvironment From Multiplex Images [J]. IEEE TRANSACTIONS ON MEDICAL IMAGING, 2023, 42(10): 3048-3058.
37. KIM G, JEON J H, PARK K, et al. High throughput screening of mesenchymal stem cell lines using deep learning [J]. SCIENTIFIC REPORTS, 2022, 12(1).
38. LANDEROS C, OH J, WEISSLEDER R, et al. Deep learning pipeline for automated cell profiling from cyclic imaging [J]. SCIENTIFIC REPORTS, 2024, 14(1).
39. MASCI A M, WHITE S, NEELY B, et al. Ontology-guided segmentation and object identification for developmental mouse lung immunofluorescent images [J]. BMC BIOINFORMATICS, 2021, 22(1).
40. MATSUDA K, UENO A, TSUZAKI J, et al. Vessels encapsulating tumor clusters contribute to the intratumor heterogeneity of HCC on Gd-EOB-DTPA-enhanced MRI [J]. HEPATOLOGY COMMUNICATIONS, 2025, 9(1).
41. MIAO K, LIN L E, QIAN C X, et al. Label-free Super-resolution Imaging Enabled by Vibrational Imaging of Swelled Tissue and Analysis [J]. JOVE-JOURNAL OF VISUALIZED EXPERIMENTS, 2022, (183).
42. NGUYEN H T, PIETRASZEK N, SHELTON S E, et al. Utilizing convolutional neural networks for discriminating cancer and stromal cells in three-dimensional cell culture images with nuclei counterstain [J]. JOURNAL OF BIOMEDICAL OPTICS, 2024, 29.
43. NOGUCHI Y, MURAKAMI M, MURATA M, et al. Microscopic image-based classification of adipocyte

differentiation by machine learning [J]. HISTOCHEMISTRY AND CELL BIOLOGY, 2023, 159(4): 313-327.